Predictive design of intrinsic half-metallicity in zigzag tungsten dichalcogenide nanoribbons

Ping Cui, Jiang Zeng, Haowei Peng, Jin-Ho Choi, Zhenyu Li, Changgan Zeng, Chih-Kang Shih, John P. Perdew, and Zhenyu Zhang

Phys. Rev. B **100**, 195304 — Published 8 November 2019

DOI: 10.1103/PhysRevB.100.195304

Predictive Design of Intrinsic Half-Metallicity in Zigzag Tungsten Dichalcogenide Nanoribbons

Ping Cui,[1] Jiang Zeng,[1] Haowei Peng,[2] Jin-Ho Choi,[3] Zhenyu Li,[1] Changgan Zeng,[1] Chih-Kang Shih,[4] John P. Perdew,[2] and Zhenyu Zhang[1,*]

[1]*International Center for Quantum Design of Functional Materials (ICQD), Hefei National Laboratory for Physical Sciences at the Microscale, and Synergetic Innovation Center of Quantum Information and Quantum Physics, University of Science and Technology of China, Hefei, Anhui 230026, China*

[2]*Department of Physics, Temple University, Philadelphia, PA 19122, USA*

[3]*Soochow Institute for Energy and Materials InnovationS (SIEMIS), College of Physics, Soochow University, Suzhou, Jiangsu 215006, China*

[4]*Department of Physics and Chemistry, The University of Texas at Austin, Austin, Texas 78712, USA*

[*]*Corresponding author: zhangzy@ustc.edu.cn*

ABSTRACT

Realization of half-metallicity with a sizeable minority-spin gap and ferromagnetic ordering has been a central research emphasis in the development of next-generation spintronic devices. To date, only three-dimensional (3D) half-metals have been achieved experimentally, while their counterparts based on 2D materials remain to be materialized despite extensive efforts based on various predictive designs. This standing challenge is largely due to stringent requirements to establish ferromagnetic order in low-dimensional systems. Here we use first-principles approaches to show that

atomically thin zigzag tungsten dichalcogenide WX_2 (X = S, Se) nanoribbons preserving the stoichiometry of W:X = 1:2 stand as highly appealing intrinsic half-metallic systems, without invoking the prevailing approaches of applying an external electric field, chemical modification, or carrier doping. The readily accessible half-metallicity is attributed to distinctly different edge reconstructions, insulating along the X-terminated edges, metallic along the self-passivated W-terminated edges, the latter further characterized by a robust spin-polarized electron transmission channel. These findings are expected to provide indispensable elemental building blocks for spintronic applications purely based on 2D materials.

PACS numbers: 72.25.-b, 72.20.-i, 73.22.-f, 75.50.-y

I. INTRODUCTION

Half-metallic materials are capable of complete spin selection, allowing electrons with one spin orientation to transport through, blocking electrons with the other spin orientation [1]. Such materials have been attracting tremendous attention in the past decades due to their potential applications in spintronics. To date, only three-dimensional (3D) half-metals have been well established [2-8], while their counterparts based on 2D materials remain to be realized despite extensive efforts based on various predictive designs [9-24]. Earlier theoretical efforts to search for half-metallicity in 2D systems have been mainly focused on light-element-based materials or systems with *sp*-valence electrons. Compelling examples include zigzag graphene nanoribbons under the application of a strong external electric field across the ribbons [9,10], proper chemical modification of the ribbon edges [11-13], or edge modification plus carrier doping [14]. On the experimental side, a definitive proof of the existence of half-metallicity in 2D systems remains to be achieved. This standing challenge is inherently tied to the fundamental limitation that ferromagnetism is hard to establish in pure light-element-based or *sp*-electron systems [25-27], while the existence of ferromagnetic ordering is an essential prerequisite for establishing half-metallicity.

Beyond *sp*-electron-based systems, 2D transition metal dichalcogenides (TMDs) [28-30] offer a new class of materials for potentially realizing half-metallicity in atomically thin systems. Such elemental building blocks are highly desirable for developing spin-based devices consisting only of layered materials [31]. Indeed, more recent predictive designs of half-metallic systems in lower (2D or quasi-1D) dimensions have expanded to materials containing transition metals, including both 2D bulk and ribboned structures [17-24]. Another compelling motivation for such research efforts on low-D half-metallicity is provided by the very recent breakthrough

experimental advances in 2D ferromagnetic materials of $Cr_2Ge_2Te_6$, CrI_3, and Fe_3GeTe_2 [32-34], making it more pressing to acquire half-metallic building blocks based on 2D materials, all of which involving transition metals. In retrospect, essentially all the well-established half-metallic systems in 3D bulk form also contain transition metals [2-8], serving as another underlying reason for the rationale of the present searching effort.

In this paper, we use first-principles calculations within density functional theory (DFT) to show that atomically thin zigzag tungsten dichalcogenide WX_2 (X = S, Se) nanoribbons preserving the stoichiometry of W:X = 1:2 stand as highly appealing intrinsic half-metallic systems based on 2D materials, without the typical invocation of an external electric field, chemical modification, or carrier doping. The readily accessible half-metallicity is attributed to distinctly different structural reconstructions along the two zigzag edges of the WX_2 nanoribbons [35], insulating along the X-terminated edges, metallic along the W-terminated edges self-passivated with S or Se; the latter characterized by a robust spin-polarized electron transmission channel. We further demonstrate that the half-metallic nature of the WX_2 nanoribbons is robust as the ribbon width varies. These findings are expected to provide indispensable elemental building blocks for spintronic applications purely based on 2D materials.

The paper is organized as follows. In Sec. II, we briefly describe the model systems and details of the DFT calculations. In Sec. III, we show the different reconstructions along the different edges of zigzag WX_2 (X = S, Se) nanoribbons, and further demonstrate their intrinsic half-metallicity. The half-metallic properties are shown to be attributable to the different structural reconstructions along the two zigzag edges, and are shown to be robust as the ribbon width varies. In Sec. IV, we make closer connections with potential application aspects of the half-metallicity in zigzag WX_2 nanoribbons and their fabrication aspects, and discuss the contrasting structural and

electronic properties for MoX_2 (X = S, Se) and WTe_2 nanoribbons. Finally, we conclude in Sec. V.

II. MODEL SYSTEMS AND METHODS

A pristine WX_2 nanoribbon is likely bounded by zigzag or armchair edges, as shown in Fig. 1(a). In this work, we focus on zigzag nanoribbons with preserved stoichiometry of W:X = 1:2 (X = S, Se). To model infinitely long zigzag nanoribbons of WX_2 with different edge reconstructions, we use 6×1 supercell geometries as highlighted in Fig. 1(b), representing WS_2 or WSe_2. The width of the nanoribbons can be varied, defined by the number of the infinitely long zigzag chains. We will hereafter label a nanoribbon containing *n* zigzag chains along the ribbon direction as an *n*-ZZ nanoribbon.

Our DFT calculations were performed using the projector-augmented wave method [36] implemented in the Vienna *ab initio* simulation package (VASP) [37,38], with the Perdew-Burke-Ernzerhof (PBE) exchange-correlation functional [39]. A plane-wave basis set was adopted with an energy cutoff of 350 eV. The 1D Brillouin zone was sampled using a 6×1×1 Monkhorst-Pack *k*-point mesh for the 6×1 supercells. For the density of states (DOS) calculations, we use the tetrahedron method (ISMEAR = -5) with a *k*-point mesh of 6×1×1, and the energy range between E_{fermi}-1 and E_{fermi}+1 is divided into 2000 intervals (NEDOS = 2000). We have also tested the convergence using much denser k-meshes of 9×1×1 and 6×3×3, which provide very similar DOS to that of 6×1×1 for both systems. In each supercell, the vacuum layers between two neighboring ribbons are thicker than 16 Å. All the atoms were fully relaxed by the conjugate gradient algorithm until the residual force components were less than 0.01 eV/Å. We have used two different approaches (namely, by varying all the simulation cell sizes or the size along the ribbon direction only) to check on the effects of constant

volume simulations, and confirmed that the overall energetics stays intact, especially with regard to relative stabilities. A canonical ensemble was adopted for *ab initio* molecular dynamics (AIMD) simulations using the algorithm of Nosé [40], with the time step of 2 fs.

The validity of the main findings has also been verified by using calculations based on the range-separated Heyd-Scuseria-Ernzerhof 2006 (HSE06) hybrid functional [41,42]. We have further confirmed that the inclusion of the spin-orbit coupling (SOC) within the systems will not alter the main picture of the present study.

III. RESULTS AND ANALYSIS

Pristine single-layered TMD systems of infinite size possess finite band gaps [28-30]. For possible emergence of spin-polarized conducting states, further reduction of the systems' dimensionality is needed. For an infinitely long ribbon with preserved stoichiometry of W:X = 1:2 (X = S, Se), the two armchair edges are semiconducting and structurally equivalent, largely preserving their bulk-terminated geometry. In contrast, the two zigzag edges are distinctly different, terminated by W and X atoms, respectively, and the zigzag ribbons are metallic [43,44]. In particular, some recent studies have reported that half-metallicity in zigzag WS_2 and WSe_2 nanoribbons can be expected by invoking chemical modification of the edges [45] or doping [46]. Furthermore, it has been recognized that the metallic nature of the zigzag edges also suggests that these bulk-terminated edges are likely to be energetically unstable; as a consequence, these two different types of zigzag edges will endure drastically different structural reconstructions [35]. Experimentally, selection of such reconstructed edges can be achieved under proper physical conditions during growth, as shown in the case of $MoSe_2$ [47]. This analysis serves as the basis for potential existence of half-

metallicity in zigzag WX_2 nanoribbons.

A. Edge reconstructions

Figure 1(b) shows the energetically most stable structures of an 8-ZZ WX_2 nanoribbon with a (2×1)-reconstructed W-terminated edge and a (3×1)-reconstructed X-terminated edge [35]. Along the W-terminated edge, the (2×1) reconstruction is characterized by place exchanges of the outmost X and W edge atoms via a self-passivation mechanism. Here, all the outmost W atoms substantially move inward and half of the outmost X atoms move outward, leading to a planar W_3 trimer with the edge W atoms all effectively passivated by the displaced X atoms. The energy gain for the W-terminated edge of WS_2 (WSe_2) is 0.807 (1.012) eV per formula unit along the edge direction relative to the unreconstructed case. In contrast, the X-terminated edges undergo a more moderate (3×1) reconstruction, characterized by slight local place readjustments of the edge atoms, with 2/3 of the W-X bonds shortened, while the other 1/3 elongated. The energy gain for the S(Se)-terminated edge of WS_2 (WSe_2) is 0.172 (0.046) eV per formula unit relative to the unreconstructed case. Overall, the energy gain of the reconstructed 8-ZZ WS_2 (WSe_2) nanoribbon is 0.940 eV (1.035 eV) per formula unit along the ribbon direction.

To examine the thermodynamic stability of the WX_2 nanoribbons, we have performed the AIMD simulations at 300 K. In these simulations, we use the 6×1 supercells to allow the systems to be restructured freely at the given temperature. The evolutions of the temperature and total energy of the 8-ZZ WS_2 and WSe_2 nanoribbons during the AIMD simulations up to 15 ps are given in Fig. 2, showing that the nanoribbons essentially preserve their ordered structures at the end of the simulations, thereby establishing their thermodynamic stability.

The chemical stability of the nanoribbons is also important in realistic situations, especially when the experimental environment is not clear enough. Here, the bare edges of the nanoribbons are accompanied by chemically unpaired electrons known as dangling bonds, leaving the systems to be very reactive. Edge reconstruction is a common remedy to reduce the dangling bond nature to some extent, through the redistribution of the electrons or formation of new chemical bonds. Indeed, for the W-terminated edges, the edge atoms are dramatically readjusted during the reconstruction and form new chemical bonds, effectively removing the dangling bonds of the edge W atoms; therefore, we expect that the reconstructed WX_2 nanoribbons in the present study would not be too chemically active. However, their exact chemical stability in the presence of other chemicals or elements still need further detailed investigation on a case-by-case basis.

B. Intrinsic half-metallicity in reconstructed zigzag WS_2 nanoribbons

Distinctively, our spin-resolved electronic structure calculations further show that an 8-ZZ reconstructed WS_2 nanoribbon is a half-metal. As a reference, Fig. 3(a) displays the spin-unresolved band structure of the 8-ZZ WS_2 nanoribbon, which has one edge state (the triply folded I band) crossing the Fermi level. Note that the 6×1 supercell adopted leads to triply folded bands for the (2×1) reconstructed W-terminated edge and doubly folded bands for the (3×1) reconstructed S-terminated edge. When spin polarization is included, this band has a sizable spin split of ~0.3 eV [Fig. 3(b)], with the spin-down component (labeled as I-d) fully occupied, while the spin-up component (I-u) partially occupied. In contrast, the rest of the bands away from the Fermi level have much smaller spin splits, and some even remain spin degenerate. As a consequence, the spin-up channel is metallic, while the spin-down channel is insulating with a pronounced spin-down (minority-spin) gap of 0.56 eV, similar to the gap opening

associated with charge density waves along the grain boundaries of TMD overlayers [48,49]. These observations clearly demonstrate the emergence of robust half-metallicity in the zigzag WS_2 nanoribbon protected by a large half-metallic gap. Energetically, the spin-resolved state is 0.105 eV per supercell lower than the spin-unresolved state, showing that the half-metallicity can be established under physically realistic conditions (such as at experimentally accessible finite temperatures). Here we also stress that the energy difference is primarily associated with the relatively few edge atoms, with the atoms in the inner region of the ribbon being irrelevant.

The half-metallicity of the WS_2 nanoribbon is reflected by the metallic states propagating only along the W-terminated edge and possessing only one spin orientation. The spin-resolved total DOS and the partial DOS (defined by summing over all the atoms of the two outmost zigzag chains along the W-terminated edge) are displayed in Fig. 3(b), indicating that the I-u band originates from the W-terminated edge. When analyzed at the atom-resolved level, the I-u band is contributed from the d_{yz} orbitals of the W atoms in the W_3 trimers and the p_y/p_z orbitals of the outmost displaced S atoms along the W-terminated edge (with the nanoribbon extending along the x direction), indicating its delocalized nature. In contrast, the II-u and II-d bands are mainly contributed from the d_{xy}, d_{x^2}, and d_{z^2} orbitals of the W atoms along the S-terminated edge with negligible contribution from the edge S atoms, indicating their truly localized nature. We also find that the bands originating from the W-terminated edge will split when spin-polarization is considered, while those from the S-terminated edge will not (e.g., the II-u and II-d bands). The spatial charge density distribution of the I-u band at the Γ point is also contrasted in Fig. 3(c), showing that the metallic states are distributed at the W-terminated edge, consistent with the conclusion of the DOS analysis.

To confirm that the half-metallic system indeed exhibits a certain type of

ferromagnetic ordering, we note that the spin-polarized triply folded I-u band around the Fermi level is quite flat, which serves as the underlying basis for possible emergence of certain collective phenomena such as long-range ferromagnetism. Our detailed analysis confirms that ferromagnetism is stabilized along the reconstructed W-terminated edge of the WS_2 nanoribbon. The total magnetic moment of the 8-ZZ WS_2 nanoribbon is calculated to be 2.0 μ_B per supercell. Figure 4(a) shows the atom-resolved distribution of the magnetic moment of the 8-ZZ WS_2 nanoribbon, displaying the dominant contributions by the ferromagnetically coupled constituent atoms along the W-terminated edge. The magnetic moments are located mainly on the outmost S atoms and inner W atoms of the reconstructed W_3 trimers along the W-terminated edge, and these two types of atoms are ferromagnetically coupled. The magnetic moments on the other two W atoms of the reconstructed W_3 trimer and on the other W atoms in the second row are roughly an order of magnitude smaller. In contrast, there is no magnetism along the S-terminated edge, which can be qualitatively attributed to the fact that the (3×1) reconstruction effectively stabilizes the S-terminated edge, making it insulating. We have also doubled the supercell size along the ribbon direction to include an even number of the W-terminated (2×1) units, allowing to consider the competition from the antiferromagnetic state, and the results confirm that the ground state remains ferromagnetic.

C. Intrinsic half-metallicity in reconstructed zigzag WSe_2 nanoribbons

Similar to the WS_2 nanoribbon, the 8-ZZ WSe_2 nanoribbon is also shown to be a half-metal, albeit with a smaller insulating gap for the minority-spin channel. Its spin-unresolved electronic structure shows a triply folded band crossing the Fermi level [Fig. 3(d)], which splits by 0.26 eV when spin polarization is included [Fig. 3(e)]. The spin-down component of band I (I-d) is fully occupied, while the spin-up component (I-u) is

partially occupied. Here, the doubly folded bands (II-u and II-d) contributed by the p_y/p_z orbitals of the Se atoms along the Se-terminated edge are much closer to the Fermi level than those for the WS_2 nanoribbon. As a consequence, the minority-spin insulating gap of 0.32 eV is substantially narrower than that for the WS_2 nanoribbon. The corresponding total DOS and partial DOS of the atoms in the W-terminated edge, as well as the spatial charge density distribution of the I-u band at the Γ point, are shown in Figs. 3(e) and 3(f), confirming that the I-u band originates from the W-terminated edge.

The ferromagnetism of the 8-ZZ WSe_2 nanoribbon is also similar to that of the 8-ZZ WS_2 nanoribbon. In particular, the total magnetic moment of the WSe_2 nanoribbon is again 2.0 μ_B per supercell, and the atom-resolved distribution of the magnetic moment is displayed in Fig. 4(b).

D. Half-metallicity within the hybrid functional method or with SOC

As a cross check, the half-metallic nature of the nanoribbons is further confirmed by band structure calculations using the HSE06 hybrid functional. The hybrid functional, as implemented with the generalized-Kohn-Sham scheme [50], can improve the band structure and band gap for insulators over the PBE functional for a right reason [51]. Comparing the band structures from the HSE06 to that from the PBE, we find that the half-metallic nature arising from the edge state qualitatively stays intact, but now with the expected larger minority-spin gaps, as shown in Figs. 5(a) and 5(b). Additionally, recent studies have also shown the importance of SOC in such TMD systems [52,53]. As yet another cross check, we have tested the SOC effects on the edge states of the WX_2 nanoribbons. The results are presented in Figs. 5(c) and 5(d), showing that the electronic structures along the edges are also preserved in the presence of the SOC. The underlying reason lies in the substantially larger exchange splittings due to the coupling

of different spin states along each edge.

E. Robustness of the half-metallicity

To further examine how robust the half-metallicity of the nanoribbons is, we have extended to systems with varying ribbon widths, as the inter-edge coupling may significantly alter the electronic and magnetic properties along the two edges. In doing so, the narrowest ribbon considered corresponds to $n = 3$, below which the two opposite edges can no longer reconstruct reasonably independently. We find that, for all the *n*-ZZ WX_2 nanoribbons with $n = 3,4,\ldots12$, the (2×1) reconstruction along the W-terminated edge and (3×1) reconstruction along the X-terminated edge are preserved, as shown in Fig. 6. The exception is the narrowest 3-ZZ WSe_2 nanoribbon, which favors a (2×1) reconstruction along the Se-terminated edge. The energy differences between the nonmagnetic and ferromagnetic states ($\Delta E_{mag} = E_{NM} - E_{FM}$) for the nanoribbons with $n = 4,5,\ldots8$ are shown in Fig. 7, where E_{NM} and E_{FM} are the energies of nonmagnetic and ferromagnetic states, respectively. The ferromagnetic states are the most stable for all the ribbons and their energies are always lower than that of the nonmagnetic states. In particular, the energy difference ΔE_{mag} increases with the ribbon width for the narrower ribbons and converges to a constant value when the ribbons are wide enough.

More intriguingly, the half-metallicity remains for the *n*-ZZ WX_2 nanoribbons as long as $n \geq 4$, but is clearly lost for the 3-ZZ WSe_2 nanoribbon, which becomes a non-magnetic semiconductor. The electronic properties of some representative nanoribbons are compared in Fig. 8. We also note that the total magnetic moments of the WX_2 nanoribbons change little as the ribbon width increases, but the minority-spin insulating gap increases slightly for the WS_2 ribbons and is insensitive to the width for the WSe_2 ribbons, as shown in Table 1. For the 3-ZZ WS_2 nanoribbon, it may still be classified

as a half-metal, but the triply folded I-u band is more distinctively gapped because of stronger inter-edge coupling.

IV. DISCUSSION

Several aspects are worthwhile to be discussed. First, though the flat nature of the spin-up bands around the Fermi level in zigzag WS_2 nanoribbons can serve as the underlying basis for possible emergence of certain collective phenomena, it may also limit the potential applications of the half-metallicity feature. The flat nature and small bandwidth for the spin-up bands are likely to result in larger effective mass and lower mobility of the spin-polarized electrons, limiting their transport performance. Therefore, compared with the zigzag WS_2 nanoribbons, the spin-up bands around the Fermi level in the WSe_2 nanoribbons possess larger dispersion and bandwidths, indicating better electronic transport properties. It is also noted that the location of the highest occupied spin channel for the WSe_2 nanoribbons is close to the Fermi level. To avoid the potential negative effects of thermal fluctuations on the half-metallicity, we can either reduce the operation temperature or dope electrons to increase the Fermi level of the systems in practical applications.

The second aspect is on the fabrication of the proposed nanoribbons. A tungsten dichalcogenide nanoribbon can be obtained via a top-down approach such as cutting using a transmission electron microscopy tip [54,55] or a bottom-up approach under confined growth geometry [56] or using molecular beam epitaxy [47]. Here we note that the zigzag WS_2 nanoribbons formed within carbon nanotubes do not seem to exhibit such dramatic (2×1) reconstruction along the W-terminated edge, likely due to the confined geometry of the tubes [56]. Therefore, to experimentally realize controlled fabrication of the proposed WX_2 nanoribbons with proper edge reconstructions, it is

vital to fine-tune the nonequilibrium growth conditions, so as to allow the step edges to fully relax via edge reconstruction at the growth front [47].

Thirdly, it is also worthwhile to contrast that, even though the Mo-terminated edges of zigzag MoX_2 (X = S, Se) nanoribbons experience similar (2×1) reconstruction, these systems are not half-metals, because the X-terminated edges are (2×1) reconstructed and stay ferromagnetically metallic as well, with states of both spin orientations crossing the Fermi level [35]. Furthermore, in the present study we have not included the WTe_2 nanoribbons, because the system in 2D bulk form prefers the semi-metallic 1T' phase [57,58], which is drastically different from the stable 2H phases of WX_2 (X = S, Se) considered here.

Finally, a variety of dislocations and grain boundaries (GBs) in TMDs have also been studied experimentally [59-61] and theoretically [see, for example, Refs. 62 and 63], exhibiting different electronic, magnetic, and transport properties from the TMD single layers including half-metallicity. Usually, the dislocations and GBs are formed during nonequilibrium growth, a process which typical lacks precise control [64]. Compared with such dislocations and GB structures, the nanoribbons presented here can be fabricated in a more controllable manner [47].

V. CONCLUSIONS

In conclusion, we have systematically investigated the electronic and magnetic properties of the zigzag WX_2 nanoribbons using state-of-the-art first-principles approaches, revealing their intrinsic and robust half-metallic properties. Ready availability of WX_2 nanoribbons through elegant control of the growth conditions during bottom-up self-assembly will allow exploration of their electronic, magnetic, and transport properties. Such advances will potentially enable experimental realization

of half-metallicity based on 2D materials, which in turn will provide indispensable elemental building blocks for future developments of spintronic devices.

Acknowledgements

This work was supported in part by the NSFC (11722435, 11634011, 61434002, 11974323, and 21421063), National Key R&D Program of China (2017YFA0303500), Strategic Priority Research Program of Chinese Academy of Sciences (XDB30000000), and the Anhui Initiative in Quantum Information Technologies (AHY170000). The HSE computations by H.P. were supported by the Center for Complex Materials from First Principles, an Energy Frontier Research Center funded by the U.S. Department of Energy, Office of Science, Basic Energy Sciences. The work of H.P. and J.P.P. was supported by the U.S. NSF (DE-SC0012575).

References

1. R. A. de Groot, F. M. Mueller, P. G. van Engen, and K. H. J. Buschow, Phys. Rev. Lett. **5**, 2024 (1983).
2. K. Schwarz, J. Phys. F: Met. Phys. **16**, L211 (1986).
3. K. P. Kämper, W. Schmitt, G. Güntherodt, R. J. Gambino, and R. Ruf, Phys. Rev. Lett. **59**, 2788 (1987).
4. J.-H. Park, E. Vescovo, H.-J. Kim, C. Kwon, R. Ramesh, and T. Venkatesan, Nature (London) **392**, 794 (1998).
5. M. Shirai, T. Ogawa, I. Kitagawa, and N. Suzuki, J. Magn. Magn. Mater. **177–181**, 1383 (1998).
6. W. H. Xie, Y. Q. Xu, B. G. Liu, and D. G. Pettifor, Phys. Rev. Lett. **91**, 037204 (2003).

7. S. A. Wolf, D. D. Awschalom, R. A. Buhrman, J. M. Daughton, S. von Molnár, M. L. Roukes, A. Y. Chtchelkanova, and D. M. Treger, Science **294**, 1488 (2001).
8. M. I. Katsnelson, V. Yu. Irkhin, L. Chioncel, and A. I. Lichtenstein, R. A. de Groot, Rev. Mod. Phys. **80**, 315 (2008).
9. Y.-W. Son, M. L. Cohen, and S. G. Louie, Nature (London) **444**, 347 (2006).
10. E. J. Kan, Z. Y. Li, J. L. Yang, and J. G. Hou, Appl. Phys. Lett. **91**, 243116 (2007).
11. O. Hod, V. Barone, J. E. Peralta, and G. E. Scuseria, Nano Lett. **7**, 2295 (2007).
12. E. J. Kan, Z. Y. Li, J. L. Yang, and J. G. Hou, J. Am. Chem. Soc. **130**, 4224 (2008).
13. F. W. Zheng, G. Zhou, Z. R. Liu, J. Wu, W. H. Duan, B. L. Gu, and S. B. Zhang, Phys. Rev. B **78**, 205415 (2008).
14. S. Dutta, A. K. Manna, and S. K. Pati, Phys. Rev. Lett. **102**, 096601 (2009).
15. A. J. Du, S. Sanvito, and S. C. Smith, Phys. Rev. Lett. **108**, 197207 (2012).
16. T. Cao, Z. L. Li, and S. G. Louie, Phys. Rev. Lett. **114**, 236602 (2015).
17. F. Wu, C. X. Huang, H. P. Wu, C. Lee, K. M. Deng, E. J. Kan, and P. Jena, Nano Lett. **15**, 8277 (2015).
18. F. Khoeini, Kh. Shakouri, and F. M. Peeters, Phys. Rev. B **94**, 125412 (2016).
19. X. L. Li, H. F. Lv, J. Dai, L. Ma, X. C. Zeng, X. J. Wu, and J. L. Yang, J. Am. Chem. Soc. **139**, 6290 (2017).
20. H. Kumar, N. C. Frey, L. Dong, B. Anasori, Y. Gogotsi, and V. B Shenoy, ACS Nano **11**, 7648 (2017).
21. M. Ashton, D. Gluhovic, S. B. Sinnott, J. Guo, D. A. Stewart, and R. G. Hennig, Nano Lett. **17**, 5251 (2017).
22. N. Mounet, M. Gibertini, P. Schwaller, D. Campi, A. Merkys, A. Marrazzo, T. Sohier, I. E. Castelli, A. Cepellotti, G. Pizzi, and N. Marzari, Nat. Nanotechnol. **13**, 246 (2018).

23. Q. S. Wu, Y. H. Zhang, Q. H. Zhou, J. L. Wang, and X. C. Zeng, J. Phys. Chem. Lett. **9**, 4260 (2018).

24. S. J. Gong, C. Gong, Y. Y. Sun, W. Y. Tong, C. G. Duan, J. H. Chu, and X. Zhang, Proc. Natl. Acad. Sci. U.S.A. **115**, 8511 (2018).

25. W. Heisenberg, Zeit. Phys. **49**, 619 (1928).

26. G. Z. Magda, X. Z. Jin, I. Hagymási, P. Vancsó, Z. Osváth, P. Nemes-Incze, C. Y. Hwang, L. P. Biró, and L. Tapasztó, Nature (London) **514**, 608 (2014).

27. H. González-Herrero, J. M. Gómez-Rodríguez, P. Mallet, M. Moaied, J. J. Palacios, C. Salgado, M. M. Ugeda, J. Y. Veuillen, F. Yndurain, and I. Brihuega, Science **352**, 437 (2016).

28. B. Radisavljevic, A. Radenovic, J. Brivio, V. Giacometti, and A. Kis, Nat. Nanotechnol. **6**, 147 (2011).

29. H. L. Zeng, J. F. Dai, J. F., W. Yao, D. Xiao, and X. D. Cui, Nat. Nanotechnol. **7**, 490 (2012).

30. Q. H. Wang, K. Kalantar-Zadeh, A. Kis, J. N. Coleman, and M. S. Strano, Nat. Nanotechnol. **7**, 699 (2012).

31. A. K. Geim and I. V. Grigorieva, Nature (London) **499**, 419 (2013).

32. C. Gong, L. Li, Z. L. Li, H. W. Ji, A. Stern, Y. Xia, T. Cao, W. Bao, C. Z. Wang, Y. Wang, Z. Q. Qiu, R. J. Cava, S. G. Louie, J. Xia, and X. Zhang, Nature (London) **546**, 265 (2017).

33. B. Huang, G. Clark, E. Navarro-Moratalla, D. R. Klein, R. Cheng, K. L. Seyler, D. Zhong, E. Schmidgall, M. A. McGuire, D. H. Cobden, W. Yao, D. Xiao, P. Jarillo-Herrero, and X. D. Xu, Nature (London) **546**, 270 (2017).

34. Y. J. Deng, Y. J. Yu, Y. C. Song, J. Z. Zhang, N. Z. Wang, Z. Y. Sun, Y. F. Yi, Y. Z. Wu, S. W. Wu, J. Y. Zhu, J. Wang, X. H. Chen, and Y. B. Zhang, Nature

(London) **563**, 94 (2018).

35. P. Cui, J. H. Choi, W. Chen, J. Zeng, C. K. Shih, Z. Y. Li, and Z. Y. Zhang, Nano Lett. **17**, 1097 (2017).
36. P. E. Blöchl, Phys. Rev. B **50**, 17953 (1994).
37. G. Kresse and J. Furthmüller, Phys. Rev. B **54**, 11169 (1996).
38. G. Kresse and D. Joubert, Phys. Rev. B **59**, 1758 (1999).
39. J. P. Perdew, K. Burke, and M. Ernzerhof, Phys. Rev. Lett. **77**, 3865 (1996).
40. S. Nosé, J. Chem. Phys. **81**, 511 (1984).
41. J. Heyd, G. E. Scuseria, and M. Ernzerhof, J. Chem. Phys. **118**, 8207 (2003).
42. A. V. Krukau, O. A. Vydrov, A. F. Izmaylov, and G. E. Scuseria, J. Chem. Phys. **125**, 224106 (2006).
43. Y. F. Li, Z. Zhou, S. B. Zhang, and Z. F. Chen, J. Am. Chem. Soc. **130**, 16739 (2008).
44. K.-X. Chen, Z.-Y. Luo, D.-C. Mo, and S.-S. Lyu, Phys.Chem.Chem.Phys. **18**, 16337 (2016).
45. F. López-Urías, A. L. Elías, N. Perea-López, H. R. Gutiérrez, M. Terrones, and H. Terrones, 2D Mater. **2**, 015002 (2015).
46. R. Z. Xu, B. L. Liu, X. L. Zou, and H.-M. Cheng, ACS Appl. Mater. Interfaces **9**, 38796 (2017).
47. Y. X. Chen, P. Cui, X. B. Ren, C. D. Zhang, C. H. Jin, Z. Y. Zhang, and C. K. Shih Nat. Commun. **8**, 15135 (2017).
48. H. J. Liu, L. Jiao, F. Yang, Y. Cai, X. X. Wu, W. Ho, C. L. Gao, J. F. Jia, N. Wang, H. Fan, W. Yao, and M. H. Xie, Phys. Rev. Lett. **113**, 066105 (2014).
49. S. Barja, S. Wickenburg, Z. F. Liu, Y. Zhang, H. J. Ryu, M. M. Ugeda, Z. Hussain, Z. X. Shen, S. K. Mo, E. Wong, M. B. Salmeron, F. Wang, M. F. Crommie, D. F.

Ogletree, J. B. Neaton, and A. Weber-Bargioni, Nat. Phys. **12**, 751 (2016).

50. F. Fuchs, J. Furthmüller, F. Bechstedt, M. Shishkin, and G. Kresse, Phys. Rev. B **76**, 115109 (2007).
51. J. P. Perdew, W. T. Yang, K. Burke, Z. H. Yang, E. K. U. Gross, M. Scheffler, G. E. Scuseria, T. M. Henderson, I. Y. Zhang, A. Ruzsinszky, H. W. Peng, J. W. Sun, E. Trushin, and A. Görling, Proc. Natl. Acad. Sci. U.S.A. **114**, 2801 (2017).
52. D. Xiao, G. B. Liu, W. X. Feng, X. D. Xu, and W. Yao, Phys. Rev. Lett. **108**, 196802 (2012).
53. X. D. Xu, W. Yao, D. Xiao, and T. F. Heinz, Nat. Phys. **10**, 343 (2014).
54. X. F. Liu, T. Xu, X. Wu, Z. H. Zhang, J. Yu, H. Qiu, J. H.; Hong, C. H. Jin, J. X. Li, X. R. Wang, L. T. Sun, and W. L. Guo, Nat. Commun. **4**, 1776 (2013).
55. J. H. Lin, O. Cretu, W. Zhou, K. Suenaga, D. Prasai, K. I. Bolotin, N. T. Cuong, M. Otani, S. Okada, A. R. Lupini, J.-C. Idrobo, D. Caudel, A. Burger, N. J. Ghimire, J. Q. Yan, D. G. Mandrus, S. J. Pennycook, and S. T. Pantelides, Nat. Nanotechnol. **9**, 436 (2014).
56. Z. Liu, K. Suenaga, Z. Y. Wang, Z. J. Shi, E. Okunishi, and S. Iijima, Nat. Commun. **2**, 213 (2011).
57. K. A. N. Duerloo, Y. Li, and E. J. Reed, Nat. Commun. **5**, 4214 (2014).
58. X. F. Qian, J. W. Liu, L. Fu, and J. Li, Sicence **346**, 1344 (2014).
59. A. M. van der Zande, P. Y. Huang, D. A. Chenet, T. C. Berkelbach, Y. M. You, G.-H. Lee, T. F. Heinz, D. R. Reichman, D. A. Muller, and J, C. Hone, Nat. Mater. **12**, 554 (2013).
60. S. Najmaei, Z. Liu, W. Zhou, X. L. Zou, G. Shi, S. D. Lei, B. I. Yakobson, J.-C. Idrobo, P. M. Ajayan, and J. Lou, Nat. Mater. **12**, 754 (2013).
61. H. J. Liu, L. Jiao, F. Yang, Y. Cai, X. X. Wu, W. Ho, C. L. Gao, J. F. Jia, N. Wang,

H. Fan, W. Yao, and M. H. Xie, Phys. Rev. Lett. **113**, 066105 (2014).

62. D. Le and T. S. Rahman, J. Phys.: Condens. Matter **25**, 312201 (2013).
63. Z. H. Zhang, X. L. Zou, V. H. Crespi, and B. I. Yakobson, ACS Nano **7**, 10475 (2013).
64. Z. L. Zhu, P. Cui, Y. Jia, S. B. Zhang, and Z. Y. Zhang, Phys. Rev. B **100**, 035429 (2019).

FIGURES AND FIGURE CAPTIONS

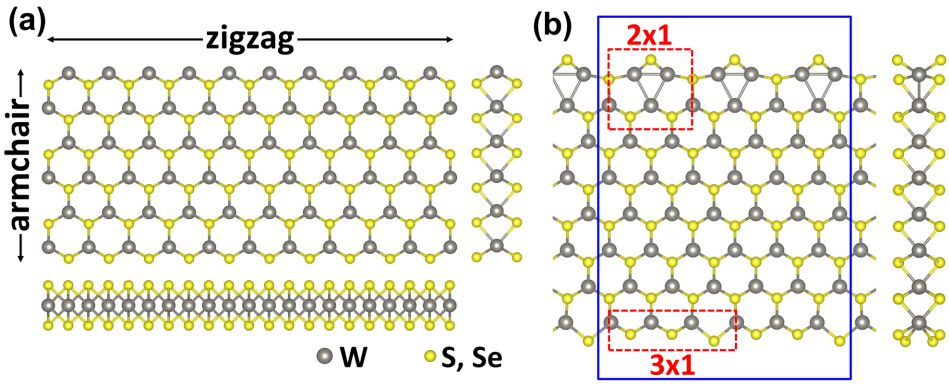

FIG. 1. (a) Top view (upper panel) and side views (right and bottom panels) of a rectangle-shaped WX_2 (X=S, Se) nanoribbon with coexisting zigzag and armchair edges. (b) Top view (left panel) and side view (right panel) of the optimized atomic structures of 8-ZZ WX_2 nanoribbons. The reconstructed structures along the W-terminated and X-terminated edges are indicated by the red dashed rectangles, respectively. The atoms included in the supercell calculations are indicated by the blue solid rectangle.

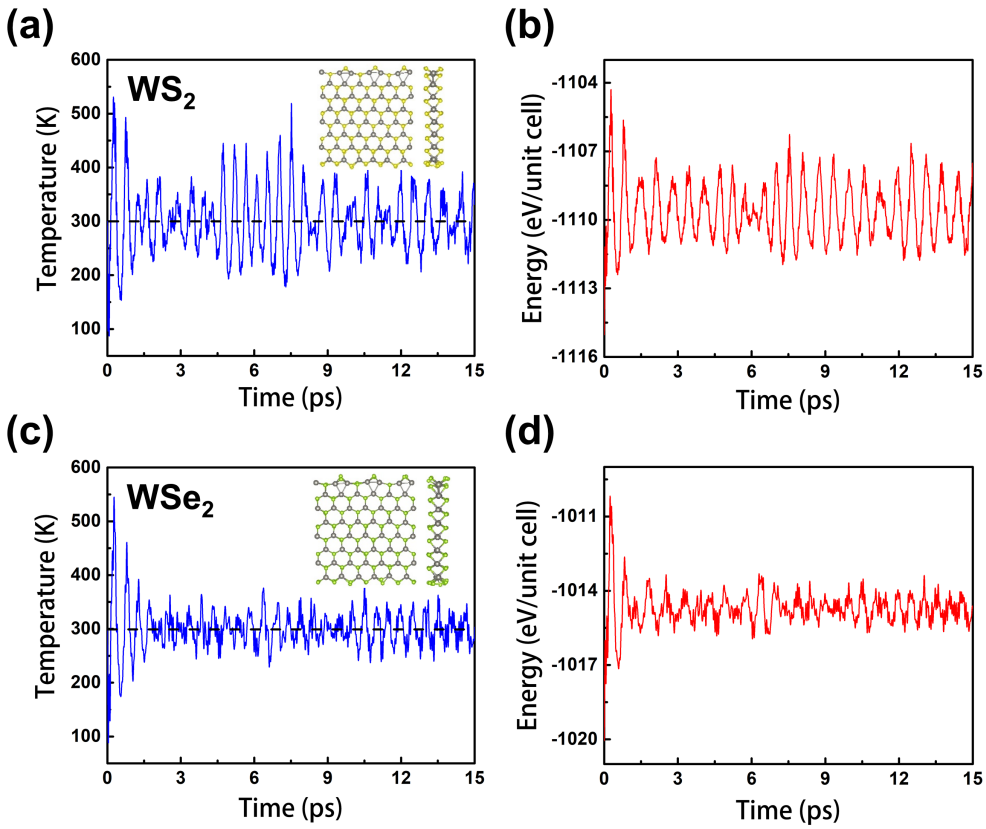

FIG. 2. (a) and (d) Spin-unresolved band structure, (b) and (e) spin-resolved band structure and DOS (including both total and partial), and (c) and (f) spatial charge density distribution of the spin-resolved tripled folded I-u band crossing the Fermi level at the Γ point of an 8-ZZ WS_2 and WSe_2 nanoribbon, respectively. The red color in the charge density plots of (c) and (f) denotes the spin-up states.

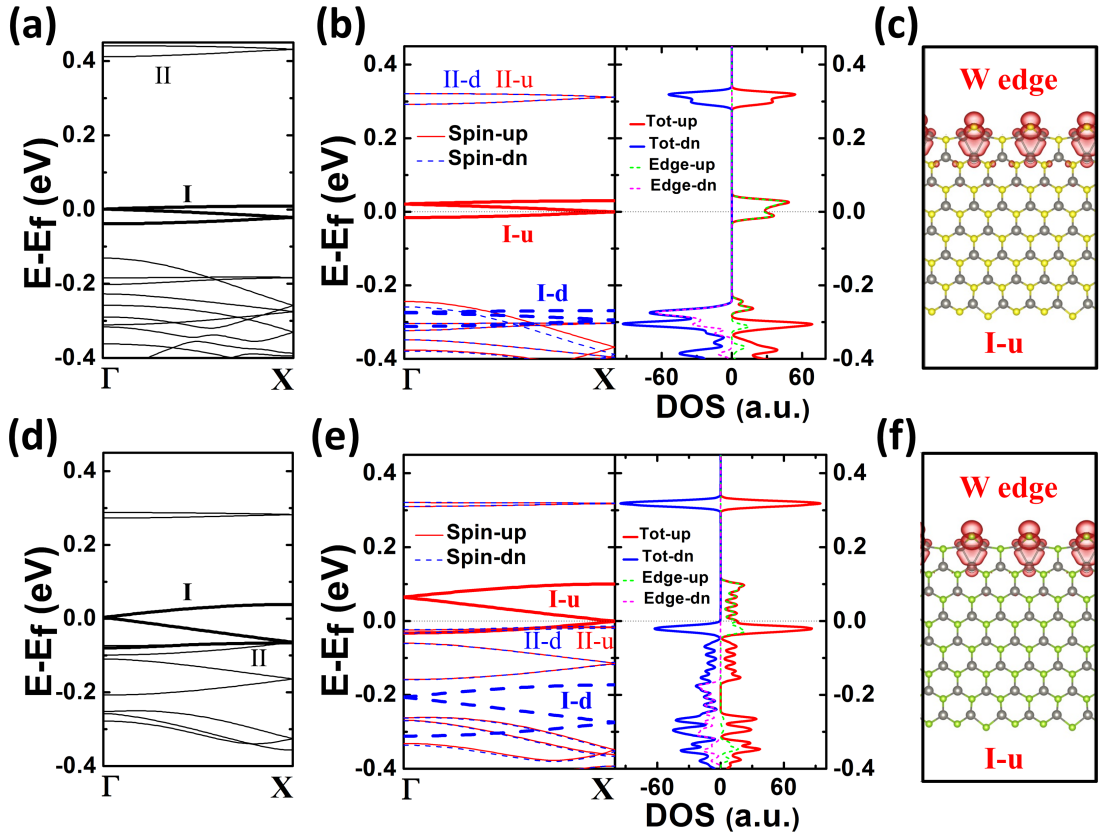

FIG. 3. (a) and (d) Spin-unresolved band structure, (b) and (e) spin-resolved band structure and DOS (including both total and partial), and (c) and (f) spatial charge density distribution of the spin-resolved tripled folded I-u band crossing the Fermi level at the Γ point of an 8-ZZ WS_2 and WSe_2 nanoribbon, respectively. The red color in the charge density plots of (c) and (f) denotes the spin-up states.

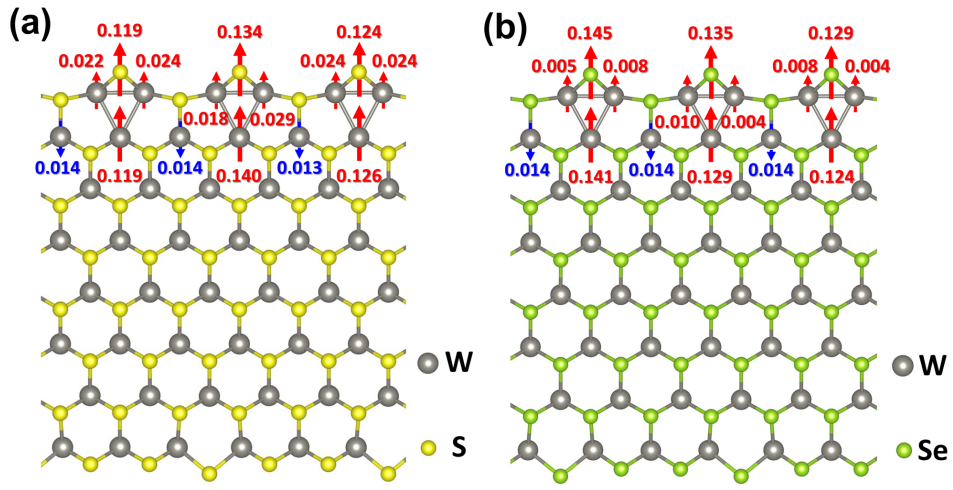

FIG. 4. Atom-resolved distributions of the magnetic moments on (a) the W and S atoms of an 8-ZZ WS_2 nanoribbon and (b) the W and Se atoms of an 8-ZZ WSe_2 nanoribbon. In both cases, only moments with absolute values > 0.005 μ_B are displayed, with the red (up) and blue (down) arrows indicating opposite spin orientations. Sizable magnetic moments are distributed on the W and X atoms along the W-terminated edges of the WX_2 nanoribbons, with no magnetism along the X-terminated edges.

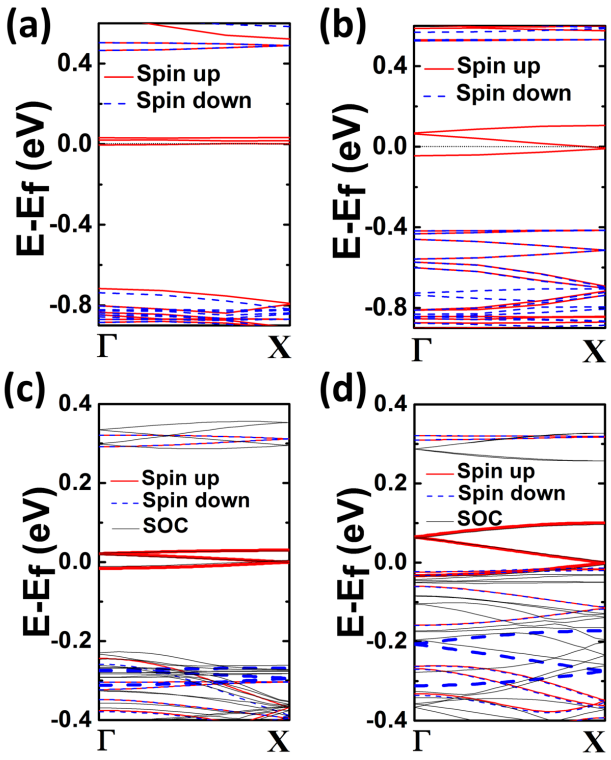

FIG. 5. Spin-resolved band structures of reconstructed 8-ZZ (a) WS_2 and (b) WSe_2 nanoribbons calculated using the HSE06 hybrid functional. Band structures of the reconstructed 8-ZZ (c) WS_2 and (d) WSe_2 nanoribbons calculated using the PBE functional with and without SOC.

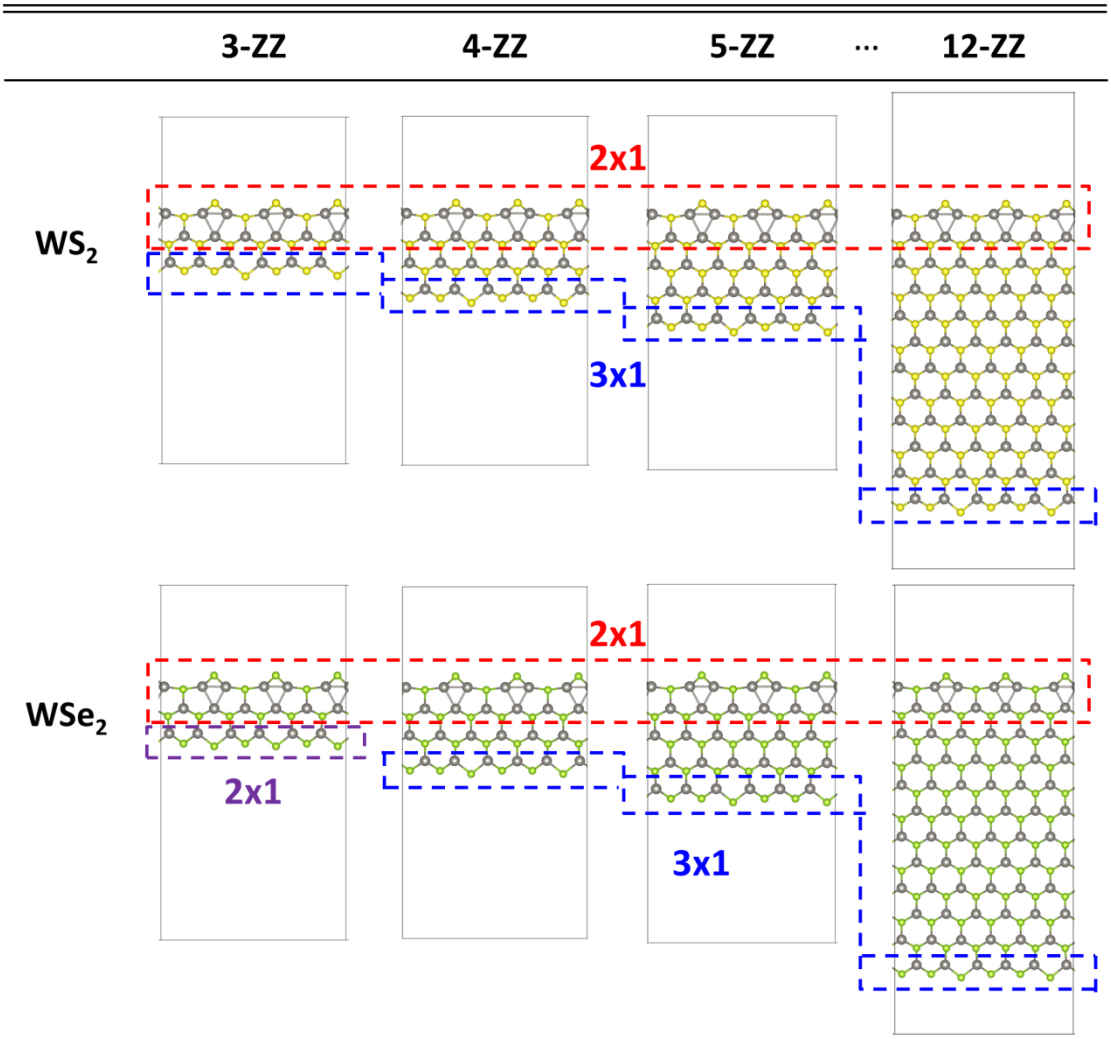

FIG. 6. Optimized structures of the reconstructed *n*-ZZ WS_2 and WSe_2 nanoribbons with $n = 3,4,5,\ldots 12$. The edge reconstructions are highlighted in the dashed rectangles.

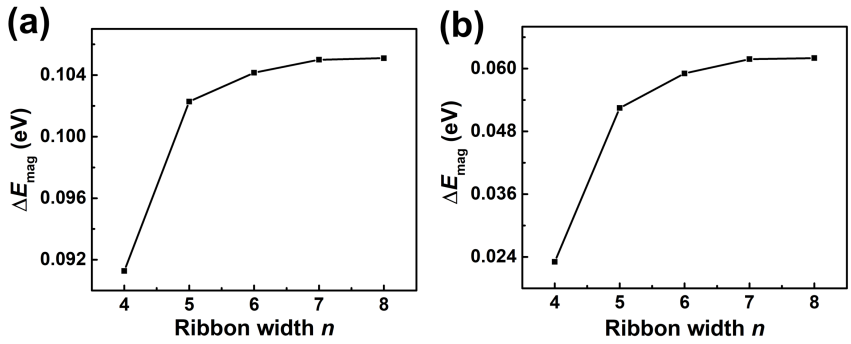

FIG. 7. Energy difference (ΔE_{mag}) between the nonmagnetic and ferromagnetic states as a function of the ribbon width (n) for the zigzag (a) WS_2 and (b) WSe_2 nanoribbons.

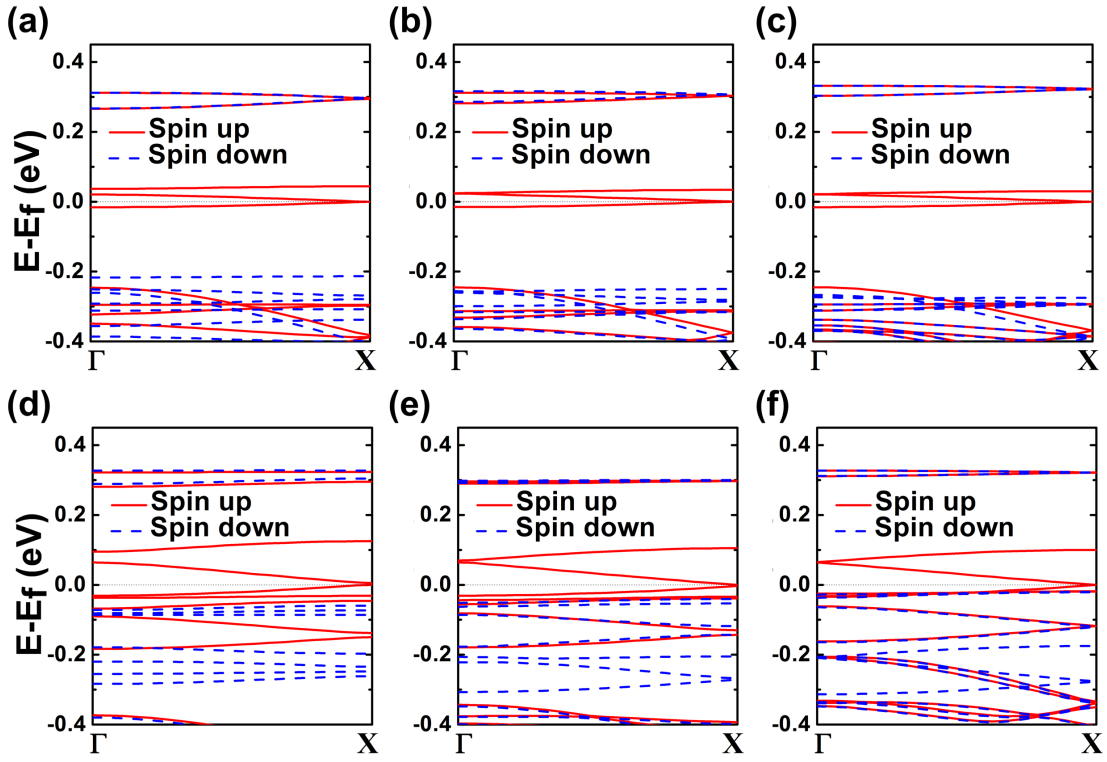

FIG. 8. Spin-resolved band structures of (a)-(c) *n*-ZZ WS_2 nanoribbons with $n = 4$, 5, and 12, and (d)-(e) *n*-ZZ WSe_2 nanoribbons with $n = 4$, 5, and 12, respectively.

Table and caption

TABLE 1.Total magnetic moment (M) and minority-spin insulating gap (ΔE_{gap}) of the n-ZZ WX_2 (X=S, Se) nanoribbons. The robust nature of the half-metallicity is displayed by the sizable and slowly varying or nearly constant ΔE_{gap} as the ribbon widens.

	WS_2		WSe_2	
	M (μ_B per supercell)	ΔE_{gap} (eV)	M (μ_B per supercell)	ΔE_{gap} (eV)
4-ZZ	2.0	0.480	2.0	0.349
5-ZZ	2.0	0.536	2.0	0.333
8-ZZ	2.0	0.561	2.0	0.324
12-ZZ	2.0	0.571	2.0	0.332